J. Iron Steel Res. Int. (2018) 25:1149–1155
https://doi.org/10.1007/s42243-018-0161-9

ORIGINAL PAPER

Hot corrosion behaviors of Super 304H austenitic stainless steel pre-coated in Na_2SO_4–25%NaCl mixture salt film

Ping Li[1] · Ting-ju Li[1] · Jie Zhao[1] · Sheng-jiao Pang[1]

Received: 14 July 2017 / Revised: 26 September 2017 / Accepted: 12 January 2018 / Published online: 19 October 2018

Abstract
Hot corrosion rates of Super 304H austenitic stainless steel pre-coated in Na_2SO_4–25%NaCl mixture salt film in air at 650 °C and 750 °C have been investigated by corrosion kinetics curves. The corrosion products are examined by means of X-ray diffraction and scanning electron microscopy coupled with energy-dispersive spectrometer, and electron probe micro-analyzer to analyze the scale structure and element distribution of the cross section. The results indicate that the kinetics curves are similar and display parabolic growth, and the mass gain obviously increases with the increasing temperature. A two-layer oxide scale composed of Fe oxides containing $CuFe_2O_4$ and Cr_2O_3 forms on the surface of the alloy and easily exfoliates with extending corrosion time or with improving corrosion temperature. Moreover, a corrosion-affected zone with micropores and micro-cracks appears beneath the oxide scale. It is concluded that the selective oxidation occurs and a protective oxide scale forms at the early corrosion stage. The melt salts destroy the integrity of the oxide scale and accelerate hot corrosion of the alloy by the cyclical oxidation–chlorination during the further corrosion processing. In addition, internal sulfidation also contributes to the corrosion of the alloy.

Keywords Ultra supercriticality · Hot corrosion · Sulfidation · Chloridation

1 Introduction

Many ultra-supercritical (USC) plants with steam temperature of ~ 600 °C and pressure of ~ 25 MPa have been built and successfully operated in the world since 1991 [1]. However, when low-grade fuels with high concentrations of sulfur, vanadium and sodium are used for firing industrial processes, the combustion products, such as alkali metal sulfates and V_2O_5 vapors, combine with other ash constituents and deposit on the cooler component surfaces, which results in severe corrosion attack [2]. The further studies indicate that high-temperature corrosion concerned with chlorine is more destructive to the alloy [3]. Shinata et al. [4] reported that when NaCl from the ocean breezes mixes with Na_2SO_4 from the fuel and deposits on the hot section of component, the corrosion of the heat-resisting alloy is accelerated and the mass loss is increased by over hundred times. Qin and Li [3] investigated hot corrosion induced by mixture of Na_2SO_4–NaCl for Ni- and Co-based superalloys and Ni–Co alloys used in turbine engines or gas turbines. Based on the investigations of the hot corrosion behavior of Ni–Cr/Ni–Co alloy induced by Na_2SO_4–25%NaCl mixture salts, the addition of 10% (wt.%, all in this paper) NaCl to the Na_2SO_4 coating can easily cause the degradation of protective Cr_2O_3 scale and increase the amount of sulfur incorporated into the substrate. It has also been reported that the ratio of Na_2SO_4 to NaCl in the mixture and the gas pressure in corrosion atmosphere have significant effect on the corrosion behaviors of the alloys, and the most severe hot corrosion on Ni- and Co-based alloy is observed at 900 °C in still air with mixtures of Na_2SO_4 containing 40% NaCl [5–10]. It is obvious that the destructive effect of chlorine on high-temperature components cannot be ignored and might have a disastrous harm on the service life of the equipments.

Among advanced materials which have been developed and applied for high-temperature and high-pressure USC components, Super 304H austenitic stainless steel with high strength and high corrosion resistance has been used

✉ Ping Li
liping69@dlut.edu.cn

[1] College of Materials Science and Engineering, Dalian University of Technology, Dalian 116024, Liaoning, China

to fabricate superheated and reheated tubes of USC fired boilers [11, 12]. The previous investigations on Super 304H are mainly concentrated on the mechanical properties and microstructure at high temperatures, and the performance in oxidizing environments is also well established [13, 14]. Unfortunately, the studies on hot corrosion behavior of Super 304H in aggressive corrosion environments, especially in the harsh environment coexisting sulfate–chloride species, have not been published extensively. Hence, the investigations on hot corrosion of Super 304H pre-coated in Na_2SO_4–25%NaCl mixture salt film in air are one of the key issues for their application in a number of combustion environments containing chlorine.

In the present study, an attempt has been made to evaluate hot corrosion behaviors and mechanism of Super 304H deposited in Na_2SO_4–25%NaCl at 650 °C and 750 °C in air. Both kinetics evolution and morphological development of the alloy are characterized and explored in detail by means of mass gain kinetics, metallographic examination and identification of corrosion products. Furthermore, the possible corrosion mechanisms are also elucidated on the basis of experimental results.

2 Experimental

The nominal chemical compositions of Super 304H used as the experimental materials in this investigation are presented in Table 1.

To facilitate hot corrosion tests, the samples were cut into rectangular specimens with the dimensions of 11 mm × 6 mm × 2 mm by a water-cooled cutting machine. Subsequently, the surfaces of the specimens were ground with SiC papers down to 800 grit, cleaned in alcohol and distilled water in an ultrasonic bath and then dried in hot air.

In order to produce the coating of fine salt particles after the water evaporated, an air gun was used to spray the saturated aqueous salt solutions on the specimen surface. The process was repeated until the dry salt particles were evenly deposited up to a total coating mass of 5 mg/cm^2. The pre-coated specimens were put into dried crucibles and then placed in a box resistance furnace. The corrosion tests were conducted in air at 650 °C and 750 °C for a regular interval, respectively. After tests, the samples were retrieved and followed by air cooling.

The mass changes (Δw) of the samples before and after corrosion tests were measured using an electronic balance with an accuracy of 0.1 mg. The exfoliated corrosion products were also measured to determine the total corrosion rate. The mass change per unit area was measured as a function of time. At least three parallel samples were measured simultaneously.

After the tests, the phase compositions of corrosion products were determined by X-ray diffraction (XRD) using monochromatic Cu Kα radiation operated at 40 kV and 100 mA. XRD data were compared with standard files proposed by Joint Committee on Powder Diffraction Standards to identify the various phases. The characterizations, composition and element distribution of the cross-sectional morphologies were investigated with scanning electron microscopy equipped with energy-dispersive spectroscope (EDS) and electron microprobe analysis techniques.

3 Experimental results

3.1 Corrosion kinetics curves of alloy

Figure 1 exhibits the mass change per unit area of the sample corroded as a function of corrosion time in air at 650 °C and 750 °C, respectively. It can be noticed that the kinetics curves of the alloy are similar and follow the parabolic growth. The hot corrosion is accelerated with the increasing corrosion temperature.

3.2 XRD analysis of corrosion products

Figure 2 illustrates XRD patterns of Super 304H corroded for 40, 100 and 200 h at 650 °C and 750 °C, respectively. Under the present experimental condition, the increasing corrosion temperature has no obvious influence on the corrosion products. Fe oxides and Cr_2O_3 are detected as the main phases of corrosion products, and a small amount of (Fe, Ni) sulfides and spinel oxides AB_2O_4 ($CuFe_2O_4$, $FeCr_2O_4$) are also discovered.

3.3 Morphology analysis and element distribution

Under the current experiment condition, a corrosion scale formed on the surface of the alloy is in poor adhesion with

Table 1 Chemical compositions of Super 304H (wt.%)

Cr	Ni	Cu	Nb	N	C	Si	Mn	P	S	Fe
17–19	7.5–10.5	2.5–3.5	0.3–0.6	0.05–0.12	0.07–0.13	≤ 0.30	≤ 1.00	≤ 0.04	≤ 0.01	Balance

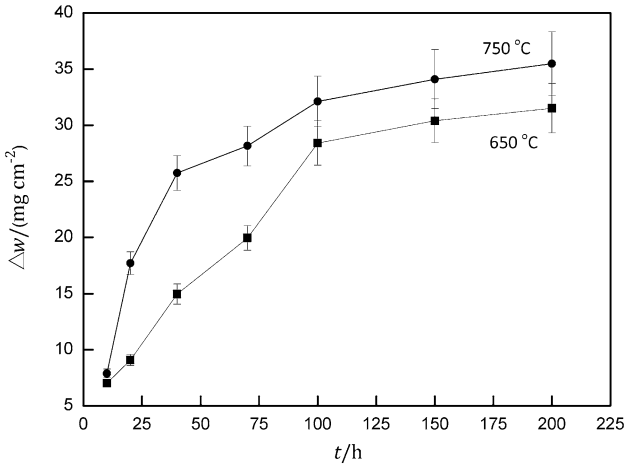

Fig. 1 Corrosion kinetics curves of Super 304H pre-coated in Na_2SO_4–25%NaCl at 650 °C and 750 °C

the matrix and is prone to exfoliate. The cross-sectional morphologies of the samples corroded for 40 h and 200 h at 650 °C are presented in Fig. 3. A two-layer corrosion scale of Fe, Cr and O enrichment determined by EDS forms on the surface of the alloy. Combining EDS results with XRD patterns, it can be deduced that the outer layer is mainly composed of Fe-enriched oxides (Fe_2O_3 and Fe_3O_4) containing $CuFe_2O_4$, and the inner layer is Cr_2O_3 combined with the spinel oxides AB_2O_4 ($CuFe_2O_4$, $FeCr_2O_4$). In addition, a rather shallow corrosion-affected zone with micropores appears beneath the oxide scale. It is observed that sulfur element mainly distributes beyond the pores, and more Ni and Fe are also detected in the region of Cr depletion. Combining with XRD results, a trace amount of sulfides form in the corrosion-affected zone about 6 μm in width, which implies that the internal sulfidation takes place in the regions. Comparing the morphology of samples corroded for 200 h (as shown in Fig. 3b) with that for 40 h, it is obvious that the alloy suffers serious corrosion attack, and the oxide scale is thickened and becomes relatively loose as well as porous. Moreover, there are more pores and micro-cracks occurring in the corrosion-affected zone with the width of 50 μm. In combination with XRD and EDS results, the phase composition and the element distribution are similar to those detected in Fig. 3a.

Figure 4 displays electron probe micro-analyzer (EPMA) of the sample corroded for 200 h at 650 °C. Based on the element distribution shown in Fig. 4, some of Fe occurs in the outer of the scale combining with a minor of Cu, Cr distributing in the inner layer, and O exists in the whole corrosion scale.

The cross-sectional morphologies of samples corroded for 40 h and 200 h at 750 °C are presented in Fig. 5. Comparing with those at 650 °C, both oxide scale and corrosion-affected zone are thickened obviously. Combining Fig. 2b with Fig. 5, it is analyzed that the corrosion scale with the thickness of 70 μm is still mainly composed of Fe oxides and Cr_2O_3 as well as spinel oxides, and more pores occur in the corrosion-affected zone with the depth of 30 μm. Extending the corrosion time to 200 h, the oxide scale becomes looser and more porous. At the same time, more cracks exist in the affected corrosion zone of Fe, Ni enrichment according to EDS results. Moreover, a trace amount of S is determined, which implies the formation of internal sulfidation in the region.

Figure 6 displays EPMA of the sample corroded for 200 h at 750 °C. The cross-sectional morphologies and

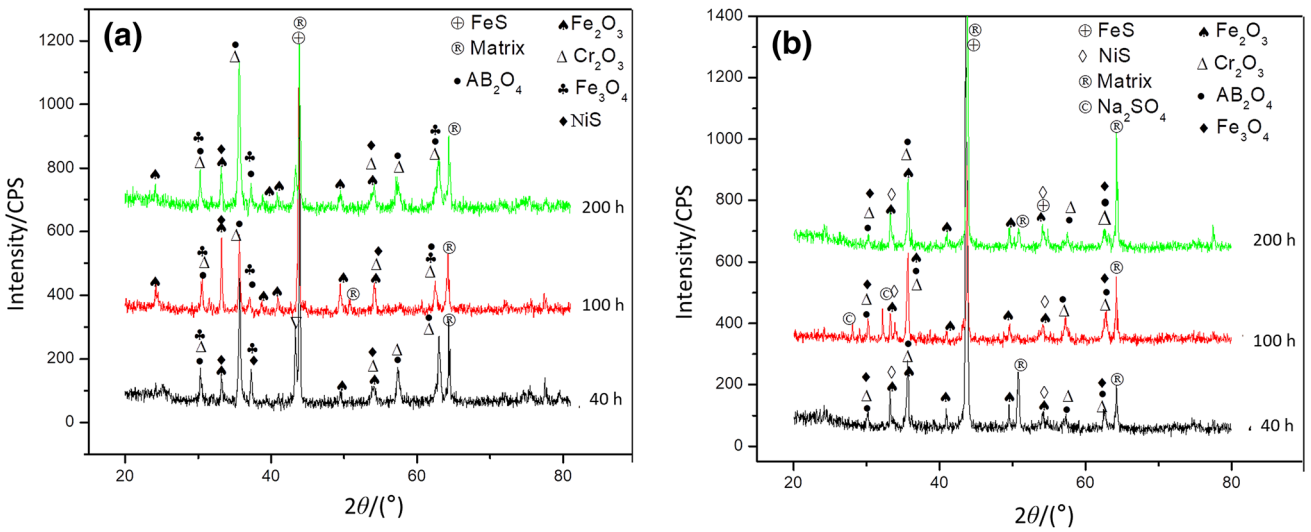

Fig. 2 XRD pattern of Super 304H pre-corroded Na_2SO_4–25%NaCl at 650 °C (**a**) and 750 °C (**b**)

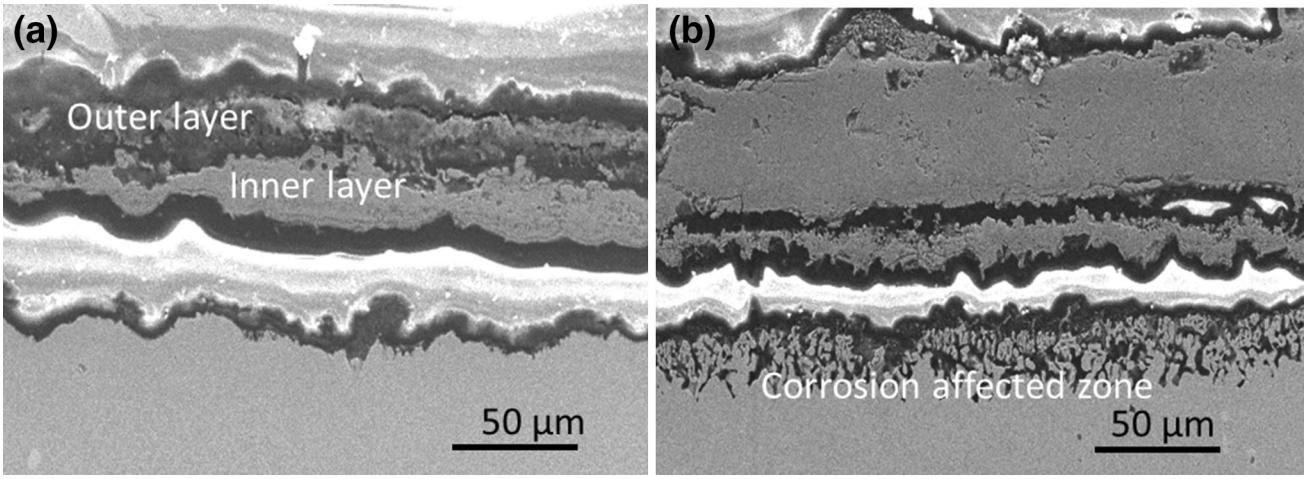

Fig. 3 Cross-sectional micrograph of Super 304H corroded in Na_2SO_4–25%NaCl at 650 °C for 40 h (**a**) and 200 h (**b**)

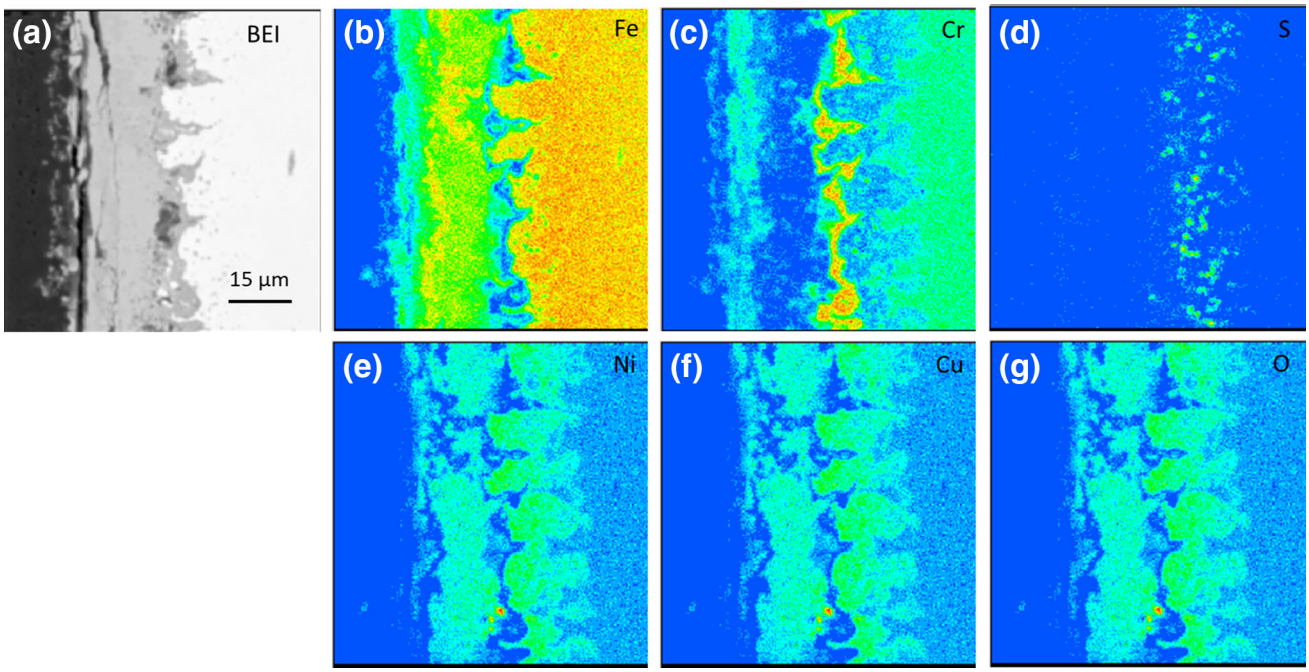

Fig. 4 EPMA analysis of Super 304H corroded in Na_2SO_4–25%NaCl at 650 °C for 200 h

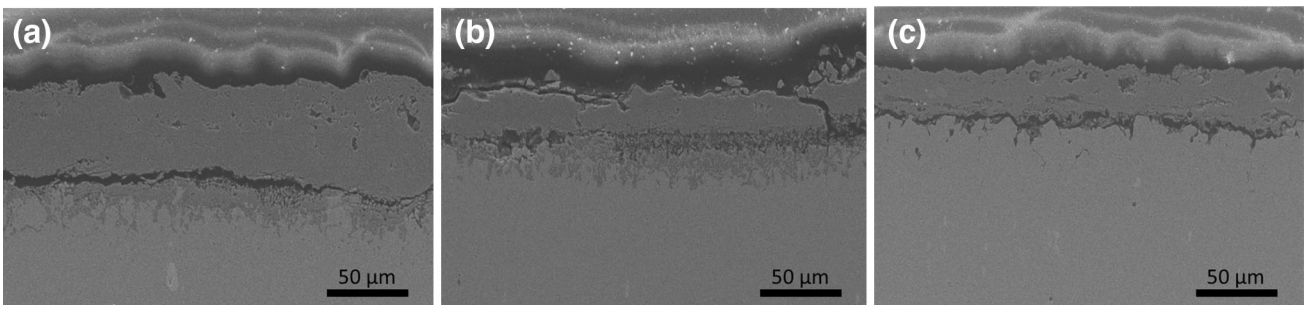

Fig. 5 Cross-sectional micrograph of Super 304H pre-coated in Na_2SO_4–25%NaCl at 750 °C for 40 h (**a**), 100 h (**b**), and 200 h (**c**)

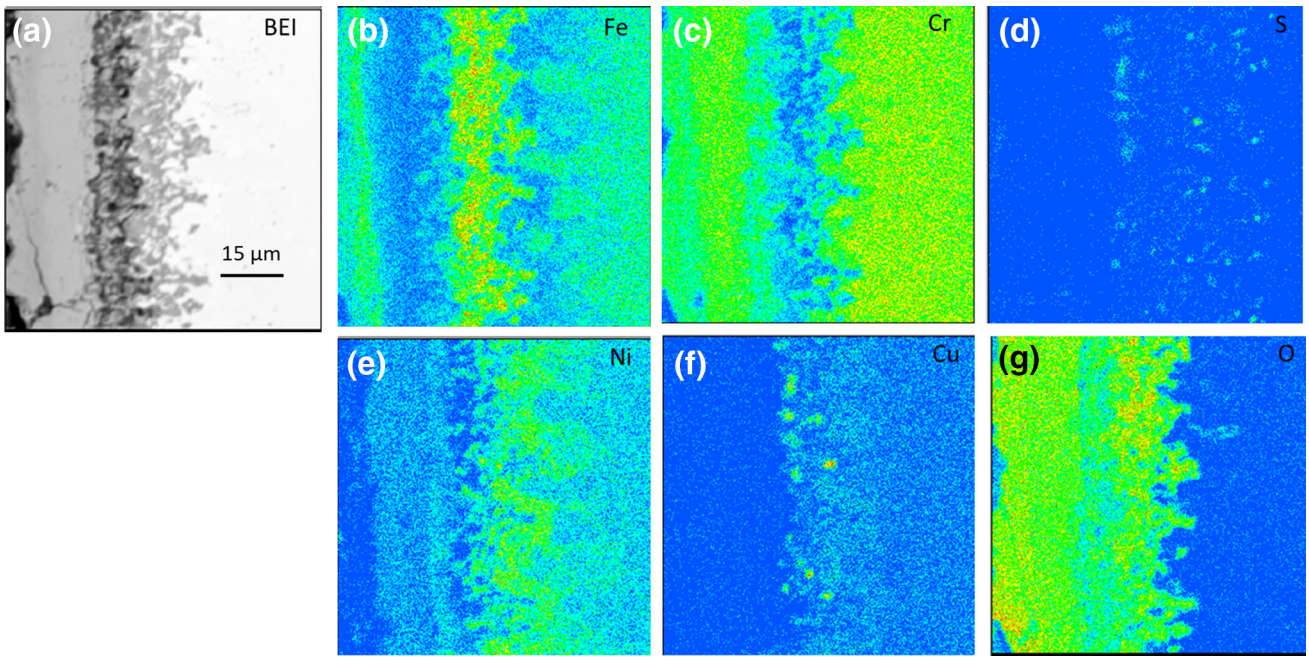

Fig. 6 EPMA of Super 304H corroded in Na_2SO_4–25%NaC1 for 200 h at 750 °C

element distribution are similar to those in Fig. 4. Most of O occurs in the oxide scale, and Cr exists in the inner of the oxide scale. Some of Fe enriches in the corrosion-affected zone besides in the outer of the oxide scale, and a trace of S is also discovered in the region.

Given all that, it is concluded that the cross section of the alloy consists of the outer oxides scale including various oxides and the inner corrosion-affected zone containing pores as well as cracks. Increasing the corrosion temperature or extending the corrosion time can accelerate the corrosion attack of the alloy, resulting that the corrosion products are prone to exfoliate from the surface of the alloy due to the poor adjacent between the oxide scale and the matrix.

4 Analysis and discussion

4.1 Selective oxidation of alloy at beginning of corrosion

Under the present experimental condition, hot corrosion of Super 304H is influenced by corrosion temperature, characteristics and species of deposition salts, etc. At the initial stage of the corrosion, the oxygen in the air passes through the mixture salt film, so a compacted and protective Cr_2O_3 oxide scale forms on the surface of the alloy by preferential oxidization. With the formation of Cr_2O_3 oxide scale, the oxygen partial pressure between the interface of the alloy and oxide scale decreases and leads to the occurrence of non-continuous Fe oxides scales. At the same time, when Cu element diffuses from the outside to the oxide surface which is under high oxygen pressure conditions, along the iron oxide grain boundary, the spinel oxide ($CuFe_2O_4$) in Cu-enriched area is produced to reduce the Gibbs free energy (ΔG) [15]. In a word, a mixed oxide scale composed of external Fe-enriched oxides containing the spinel oxide ($CuFe_2O_4$) and internal Cr-enriched oxide grows on the surface of the alloy to protect the alloy against the salt mixture.

4.2 Cyclical chloridation–oxidation of alloy

The mixture salt melting point is no more than 650 °C when the ratio of Na_2SO_4 to NaCl in the mixture salt reaches 3:1 [16], so the localized melting of mixture salt can occur on the surface of the alloy and lead to the accelerated corrosion of Super 304H by cyclical chloridation–oxidation process in the present study.

On the one hand, the molten NaCl in corrosion medium destroys the protective Cr_2O_3 layer by passing through the oxide film and reacting directly with the former Cr_2O_3 at the beginning of the corrosion. On the other hand, Fe and Cr can dissolve into the molten salt and react with the molten NaCl [17]. According to the calculation of thermodynamic data, the possible reactions are listed as below [18–20].

$$4NaCl + Cr_2O_3 + 5/2O_2 \rightarrow 2Na_2CrO_4 + 2Cl_2 \quad (1)$$

$$Cr/Fe + NaCl + O_2 \rightarrow Na_2CrO_4/NaFeO_2 + Cl_2 \quad (2)$$

According to the thermodynamics data, Cr has the greatest driving force to react with chlorine and forms chloride compared with Fe as well as Ni, and nickel has the least tendency to react with chlorine and is apt to be left in the alloy substrate. Hence, Cl_2 formed in the above reactions, further diffuses inward through the pores and generates chlorides by the reaction with elements Fe and Cr according to the following reactions (3) and (4):

$$2Cr + 3Cl_2 \rightarrow 2CrCl_3 \quad (3)$$

$$2Fe + 3Cl_2 \rightarrow 2FeCl_3 \quad (4)$$

The oxides are the ultimate stable phase in the oxygen–metal–chlorine system, which enables the occurrence of oxidation reaction between metal chlorides and oxygen as reaction (5) when the former chlorides with high vapor pressure volatilize to an area with essential activity of oxygen, so the chlorides are oxidized once again to oxides and Cl_2. Compared with iron chloride, the reaction of chromium chloride with O_2 has least ΔG, which resulted in the preferential formation of the chromium oxide and subsequently iron oxides generating and covering on the top of chromium oxide.

$$2x(Fe, Cr)Cl_3 + yO_2 \rightarrow 2(Fe, Cr)_xO_y + 3xCl_2 \quad (5)$$

Cl_2 generated in above reaction (5) can be recycled according to the above reactions (3) and (4), which accelerates hot corrosion of the alloy. In a word, the molten salt NaCl as catalyst accelerates the corrosion of the alloy during cyclical chloridation and oxidation processing under the experimental conditions.

It is noted that various volatile products, such as chlorine and chlorides formed during corrosion, damage the compactness and integrality of oxide scale, resulting in the existence of more voids in oxide scale and the formation of a uniform interconnecting void-oxide network, as shown in Fig. 5, which is helpful to provide more tunnels for the diffusion inward of sulfur to the matrix and accelerate the occurrence of internal sulfidation.

4.3 Internal sulfidation of alloy

The element sulfur at first exists in the form of sulfate on the surface of the alloy in this experiment. Combining XRD pattern and EPMA results, a trace of sulfur is detected and minor of sulfides are formed in the corrosion-affected zone, which implies that element sulfur has diffused to the matrix through the oxide scales and the internal sulfidation takes place. The above phenomena could be explained as follows.

On one hand, sulfate ions in the molten salts are reduced by the chemical reaction (6); on the other hand, the continuous formation of the oxides on the surface of the alloy lowers the oxide potential in the salt and increases the sulfur potential at the beginning of the corrosion, which leads to that the released S would transport through the inevitable defects in oxide scale, reach the affected zone and react with alloying elements to produce sulfides in corrosion-affected zone.

$$2SO_4^{2-} \rightarrow 2O^{2-} + 3O_2 + 2S \quad (6)$$

Compared with elements Ni or Fe, Cr has a high affinity with sulfur and can form more stable sulfides [21]. However, due to the preferential chloridation/oxidation of Cr, Fe/Ni is prone to be left in the corrosion-affected zone and reacts with sulfur to form the sulfides of (Fe, Ni) as detected by XRD. The possible reaction is listed as below:

$$x(Fe/Ni) + yS \rightarrow (Fe/Ni)_xS_y \quad (7)$$

5 Conclusions

1. The corrosion kinetics curves are similar and follow parabolic law under the current experimental condition, and the mass gain increases obviously with the increasing temperature.
2. Fe- and Cr-enriched oxides are detected as the main phases of corrosion products. In addition, a small amount of (Fe, Ni) sulfide and spine oxides AB_2O_4 ($CuFe_2O_4$, $FeCr_2O_4$) are also discovered. The cross section is divided into the mixed oxide scale consisting of various oxides and the corrosion-affected zones containing a large number of micropores and minor of sulfides.
3. At the earlier stage of the corrosion, the selective oxidation induces the formation of the protective oxide scale. During the further corrosion processing, the molten NaCl destroys the protective oxide scales and accelerates the development of hot corrosion by cyclical chloridation and oxidation. In addition, the molten Na_2SO_4 causes the occurrence of internal sulfidation by the reaction of S from sulfate ion decomposed with Fe as well as Ni.

Acknowledgements The work was supported by the National Natural Science Foundation of China (Grant Nos. 51171037, 51134013 and U1610256).

References

[1] A. Iseda, H. Okada, H. Sembaan, M. Igarashi, Energy Mater. 2 (2007) 199–206.
[2] G.Y. Lai, High temperature corrosion of engineering alloys, American Society for Metals, Metals Park, Ohio, 1990.
[3] T.S. Qin, S.S. Li, Coal 2 (2001) 42–52.

[4] Y. Shinata, F. Takahashi, K. Hashiura, Mater. Sci. Eng. 87 (1987) 399–405.
[5] Y. Bourhis, C. St John, Oxid. Met. 9 (1975) 507–528.
[6] Y. Niu, F. Gesmundo, T.F. Viani, W. Wu, Oxid. Met. 42 (1994) 265–284.
[7] N. Hiramatsu, Y. Uematsu, T. Tanaka, M. Kinugasa, Mater. Sci. Eng. A 120–121 (1989) 319–328.
[8] Y.H. Shu, F.H. Wang, W.T. Wu, Oxid. Met. 54 (2000) 457–471.
[9] Y. Shu, F. Wang, Oxid. Met. 59 (2003) 201–204.
[10] D.M. Johnson, D.P. Whittle, J. Stringer, Corros. Sci. 15 (1975) 721–739.
[11] R. Viswanaathan, R. Purgert, U. Rao, Int. J. Pres. Ves. Pip. 83 (2006) 778–783.
[12] A. Iseda, in: Proc. 14th Conference on 'Electric power supply industry', CEPSI, Fukuoka, Japan, 2002, pp. 350–355.
[13] L.L. Wang, L.H. Zhu, Q.J. Wang, Trans. Mater. Heat Treat. 32 (2011) 127–131.
[14] G.D. Smith, H.W. Sizek, Corrosion 2000, NACE International, Houston, Orlando, Florida, 2000.
[15] J.H. Kim, D.I. Kim, J.H.Shim, K.W. Yi, Corros. Sci. 77 (2013) 397–402.
[16] D. Deb, S. RamakrishnaIyer, V.M. Radhakrishnan, Mater. Lett. 29 (1996) 19–23.
[17] A.U. Seybolt, Oxid. Met. 2 (1970) 161–171.
[18] C.C. Tsaur, J.C. Rock, C.J. Wang, Y.H. Su, Mater. Chem. Phys. 89 (2005) 445–453.
[19] O. Knacke, O. Kubaschewski, K. Hesselmann, Thermomechanical properties of inorganic substances, Springer-Verlag, Berlin, Heidelberg, 1991.
[20] Y. Shinata, Oxid. Met. 27 (1987) 315–320.
[21] S.Q. Zhao, X.S. Xie, G.D. Smith, S.J. Patel, Mater. Chem. Phys. 90 (2005) 275–281.